INTERNATIONAL JOURNAL FOR NUMERICAL METHODS IN FLUIDS
*Int. J. Numer. Meth. Fluids* 2003; **43**:1301–1328 (DOI: 10.1002/fld.541)

# Distributed parallel computation for complex rotational flows of non-Newtonian fluids

A. Baloch[†] and M. F. Webster[*,‡]

*Institute of Non-Newtonian Fluid Mechanics, Department of Computer Science, University of Wales Swansea, Singleton Park, Swansea SA2 8PP, Wales, U.K.*

SUMMARY

Complex rotational flows of non-Newtonian fluids are simulated through finite element methods. The predictions have direct relevance to dough kneading, associated with the food industry. The context is taken as two-dimensional and one of stirring material within a cylindrical vessel. Three stirrer shapes are considered, placed in eccentric location with respect to the cylinder centre. The motion is driven by the rotation of the outer vessel wall. Variation with change in rheology and change in stirrer shapes are analysed, with respect to flow kinematics, stress fields, rate-of-work and power consumed. Computations are performed for Newtonian, shear-thinning and viscoelastic fluids, at various viscosity levels to gradually approximate more realistic dough-like response. For viscoelastic fluids, Phan-Thien/Tanner constitutive models are adopted. The numerical method employed is based on a finite element semi-implicit time-stepping Taylor–Galerkin/pressure-correction scheme, posed in a cylindrical polar co-ordinate system. Simulations are conducted via distributed parallel processing, performed on a networked cluster of workstations, employing message passing. Parallel performance timings are compared against those obtained working in sequential mode. Ideal linear speed-up with the number of processors is observed for viscoelastic flows under this coarse-grained implementation. Copyright © 2003 John Wiley & Sons, Ltd.

KEY WORDS: distributed computation; finite element method; rotating flow; non-Newtonian fluids; viscoelastic; dough; work done

## 1. INTRODUCTION

In this study we consider complex rotational flows of viscous and viscoelastic fluids passed a stationary stirrer and within a cylindrical vessel. The problem is idealized from dough kneading, where the stirrer is located on the vessel lid and positioned in an eccentric location with respect to the axial axis of the vessel. The motion is driven by the vessel wall. Simulations are performed in two dimensions, representing a horizontal slice through the vertical-standing

* Correspondence to: M. Webster, Department of Computer Science, University of Wales Swansea, Singleton Park, Swansea SA2 8PP, U.K.
† E-mail: a.baloch@swansea.ac.uk
‡ E-mail: m.f.webster@swansea.ac.uk

Contract/grant sponsor: UK EPSRC; contract/grant number: L14916

*Received 16 September 2002*
*Revised 11 February 2003*

vessel and ignoring end-effects. A parallel Petrov–Taylor–Galerkin/pressure-correction scheme is employed, that involves time-stepping and finite element procedures.

The objective is to systematically analyse the influence of stirrer-shape and variation in rheology, assessing how this impinges upon flow structure, rate-of-work generated and power consumption. The corresponding implications for dough kneading are explored. Optimization of dough kneading is the goal through build-up of material structure, achieved by maximizing local rate-of-work done per unit of power. Three different stirrer-shapes are considered: full, half-horizontal and half-vertical. Computations are performed for Newtonian, shear-thinning (Carreau model) and viscoelastic fluids (Phan-Thien/Tanner models, PTT). Material ranges cover model fluids, model doughs, and dough-like fluids. The viscoelastic models incorporate some degree of strain-softening into the representative fluid properties.

Our earlier work in this area has lead in the direction of fully three-dimensional viscous flows [1], transient free-surface viscous flows [2], and viscoelastic flows with one- and two-stirrer mixer designs [3]. See also Reference [4], concerning the related topic of three-dimensional swirling flows in a cylindrical vessel driven by the motion of the vessel lid. That work demonstrated change in vortex patterns with rise in inertia and also the influence of elasticity. In our previous viscoelastic studies [5], we utilized two different types of Phan-Thien/Tanner models (linear, LPTT, and exponential, EPPT) for two sets of material parameters. For model fluids (low elasticity number), this allowed us to incorporate independently shear-thinning, strain-softening/hardening and elastic properties, and compare their relative influence upon flow behaviour, localized rate-of-work and power consumption. Also, the effects of increasing rotational vessel speed were investigated. For the one-stirrer problem, our observations were that elastic contributions dominated viscous ones in both rate-of-work and power. The larger the strain-hardening response, the greater the power accrued. Local maxima in stress differential were large (twice that of two-stirrer case) and localized influences dominated. In contrast, for the two-stirrer problem, shear influences tended to dominate locally, so that localized rate-of-work of viscous and elastic contributions were of comparable order. Nevertheless, due to more global dispersal of stress the global power doubled for the two-stirrer problem over the one-stirrer case.

Industrial flows with viscoelastic materials presents many interesting and challenging problems. To compute such industrial-scale flow problems requires huge computational recourse. This has lead to the advent of parallel computation. Recent advance in this area with both hardware and software technology, has given rise to the serious possibility of distributed computation, utilising message passing for interprocessor-communication. In this manner, massive problems become tractable, by appealing to parallel algorithms and increasing the number of processors within a defined network-cluster. Two such public-domain (supported) systems for message passing are message passing interface (MPI) [6] and parallel virtual machine (PVM) [7]. For our parallel implementations, we ensure uniform load distribution between sub-problems, using a recursive spectral bisection (RSB) domain decomposition technique, and appeal to PVM as our preferred message passing protocol. In this fashion, both homogeneous and heterogeneous network-clusters of work-stations have been tested, on two different Unix operating systems [5, 3].

To place the present work into context with respect to viscoelastic flows, solving associated algebraic linear systems of equations constitutes a large proportion of CPU time overhead. The discrete problem may be posed in either coupled form, leading to large system matri-

 

ces, or alternatively, in decoupled mode which may be handled iteratively. In the viscoelastic domain, examples of using PVM for parallelizing numerical codes are described in References [8–11]. In Reference [8], two-dimensional steady-state solutions for entry flow and stick–slip flow problems were obtained employing POLYFLOW code with a finite element algorithm. A non-linear system of partial differential equations of mixed-type KBKZ integro-differential equations was solved over unstructured triangular meshes. Both coupled and decoupled system approaches were contrasted, with a dual Schur complement technique to solve the algebraic linear systems involved. In Reference [9], a time-stepping finite volume method was used. Results were presented for the solution of flow past a cylinder between two parallel plates, employing an exponential PTT model, unstructured triangular meshes, and a decoupled solution procedure. The algebraic linear system of equations was solved sequentially through a SIMPLER iteration procedure with an explicit Gauss–Seidel solver. As in the preset work, RSB domain decomposition was recommended for mesh partitioning. Both References [8, 9] used PVM on MIMD parallel computers within a master/slave network configuration. Intel IPSC/860 hypercube and convex meta series shared-memory platforms were used by Reference [8], whilst DEC-alpha clusters were used by Reference [9]. With a fixed mesh, the performance of the above [8, 9] parallel implementations were presented demonstrating monotonically increasing speed-up and decreasing efficiency with increased numbers of processors. Results were also shown on a fixed number of processors, illustrating increase in speed-up and efficiency with increased problem size.

In References [10, 11], we described the parallel implementation of the present TGPC algorithm for inelastic fluids and flow past a rigid sphere in a tube employing unstructured meshes. Parallelisation was achieved via FORTRAN 77 code, using PVM on a cluster of diskless Sun Sparc-1 workstations, based upon paradigms of domain decomposition and a degree-of-freedom approach. A hybrid solution method was adopted, that involved a direct Choleski factorization for the pressure stiffness matrix and an iterative approach for the momentum equations. Parallel efficiency close to linear was achieved. In a further article [5], we described how the algorithm was implemented in parallel via FORTRAN 90 code for viscoelastic fluids using differential constitutive models of single-mode type. There, we dealt with three-dimensional flows, both within lid-driven cavities and between concentric rotating cylinders. The lid-driven cavity flow is a popular benchmark problem, industrially relevant for processing applications such as in coatings with short-dwell coaters and general coating processes (i.e. flexible blade, roller, and packing tape coating). The concentric rotating cylinder problem is a simplified flow, considered as a precursor to more complex stirring problems, relevant to the food industry. Results were presented for these relatively large problems, providing benchmark characteristics for the parallel implementation. Once more, metrics of speed-up and parallel efficiency revealed attractive linear performance on different sized meshes and network configurations.

Eccentric rotating cylinder problems arise in other context, such as that of the journal bearing problem, where aspect ratios between outer and inner cylinders may be high. Examples of such solutions for viscoelastic fluids, lie in References [12, 13] with finite element methods and Reference [14] with spectral element methods. In this context, the studies of Dris and Shaqfeh [12, 13] revealed purely elastic flow instabilities. Velocity profiles varied as a function of eccentricity, azimuthal coordinate, and the ratio of cylindrical rotation rates. Global effects drastically altered the hoop stresses in the base flow and the onset of flow instabilities was shown to be the result of non-local effects.

 

With respect to appropriate constitutive equations for dough, we cite two theoretical papers that deal with flour/water dough-mixtures and oscillatory flows [15, 16]. In Reference [15] a constitutive equation is proposed to represent rubber-like dough material response with strain-softening behaviour. Good agreement was reached between relaxation spectra and derived data for their model and original data available for this material. In a second article [16], and with the derived constitutive model, these authors confirm agreement between experiments and predictions in large-amplitude oscillatory shear flow. This work provides some pointers as to the more appropriate properties to inherit in representing the response of some dough-like materials. In this regard, present modelling strives to be qualitative, but for more complex flows.

The outline of the current paper follows an introduction to the flow problem, its specification and discretization, a detailed discussion upon the parallel algorithm and its implementation, prior to the analysis of our solutions and timings. We close with our reflections upon the implications of our findings with respect to the background foods processing problem.

## 2. FLOW EQUATIONS

Incompressible non-Newtonian fluid flow can be represented through an equation system comprising of equations to govern momentum transport, conservation of mass and a constitutive law for the state of stress. In the absence of body forces and under isothermal conditions such a system can be represented via a statement for the conservation of mass viz.,

$$\nabla \cdot \mathbf{u} = 0 \tag{1}$$

and for momentum transport,

$$\rho \frac{\partial \mathbf{u}}{\partial t} = \nabla \cdot \sigma - \rho \mathbf{u} \cdot \nabla \mathbf{u} \tag{2}$$

where, $\mathbf{u}$ is the fluid velocity vector field, $\sigma$ is the Cauchy stress tensor, $\rho$ is the fluid density, $t$ represents time and $\nabla$ the spatial differential operator. The Cauchy stress tensor can be expressed in the form:

$$\sigma = -\mathbf{p}\delta + \mathbf{T_e} \tag{3}$$

where $p$ is the isotropic fluid pressure, $\delta$ is the Kronecker delta tensor, and $\mathbf{T_e}$ is the total stress tensor.

For constant viscosity ($\mu$) Newtonian fluids,

$$\mathbf{T_e} = 2\mu\mathbf{d} \tag{4}$$

where the rate-of-strain tensor $\mathbf{d} = \frac{1}{2}[\nabla\mathbf{u} + (\nabla\mathbf{u})^{\dagger}]$, and $\dagger$ represents the transpose operator. For a generalized non-Newtonian or inelastic fluid, $\mathbf{T_e}$, can be represented as

$$\mathbf{T_e} = 2\mu(\dot{\gamma})\mathbf{d} \tag{5}$$

where $\mu(\dot{\gamma})$ is the viscosity function, dependent upon the shear-rate ($\dot{\gamma}$). For the Carreau model, the viscosity representation takes the form

$$\mu(\dot{\gamma}) = \mu_\infty + \frac{\mu_0 - \mu_\infty}{1 + (k\dot{\gamma})^m} \tag{6}$$

 

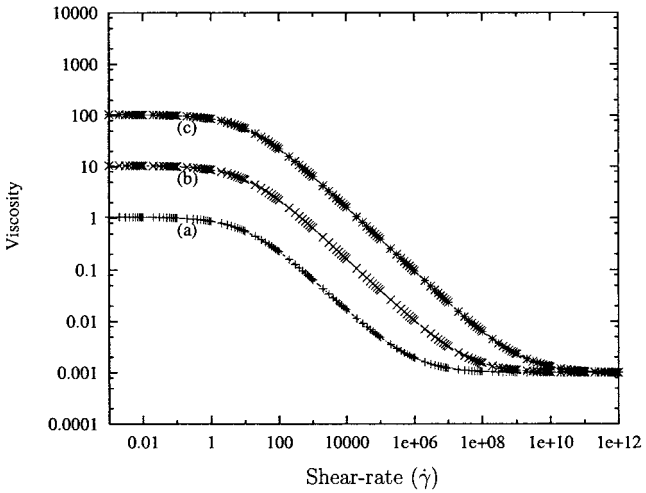


Figure 1. Carreau model viscosity: (a) $\mu_0 = 1.05$; (b) $\mu_0 = 10.5$; and (c) $\mu_0 = 105$ Pa s ($m = 0.62$, $k = 0.083$, $\mu_\infty = 0.001$).

where $\mu_0$ and $\mu_\infty$ are the zero shear-rate and second Newtonian plateau viscosities (see Figure 1), respectively, and $m$ is a power-law index. In all viscosity plots, units refer to Pa s with reciprocal seconds on shear-rate.

The upper-convected Phan-Thien/Tanner differential constitutive model, with total stress tensor $\mathbf{T_e}$, may be expressed as

$$\mathbf{T_e} = 2\mu_2\mathbf{d} + \boldsymbol{\tau} \tag{7}$$

$$\lambda_1 \overset{\nabla}{\boldsymbol{\tau}} + f\boldsymbol{\tau} = 2\mu_1\mathbf{d} \tag{8}$$

where $\boldsymbol{\tau}$ is the polymeric extra stress tensors, $\mu_1$ and $\mu_2$ are corresponding fractional viscosity splits, of polymeric and solvent type, and $\lambda_1$ is a relaxation time. Then, a total viscosity $\mu = \mu_1 + \mu_2$. The non-linear function $f$ of Equation (8) is defined as

Exponential version: $f = \mathrm{e}^{(\varepsilon\lambda_1/\mu_1)\mathrm{Tr}(\tau)}$

where $\mathrm{Tr}(\tau)$ is the trace of the polymeric stress tensor and $\varepsilon$ is a material parameter. In our present work with the exponential Phan-Thien/Tanner model, we select a parameter level of $\varepsilon = 0.25$, and adopt the notation EPTT(0.25). This model variant supports a shear-thinning response in pure shear ($\mu_s(\dot{\gamma})$ of Figure 2). In uniaxial extensional flow, EPPT(0.25) displays strain-softening, see $\mu_e(\dot{\varepsilon})$ of Figure 3.

## 3. PROBLEM SPECIFICATION

Three different problems are investigated, with a rotating vessel and a single eccentrically positioned stirrer, with respect to the vessel axis. Each problem represents a change in shape of stirrer. The first such problem is that with full-stirrer (E-F1S). Subsequently, two alternative

 

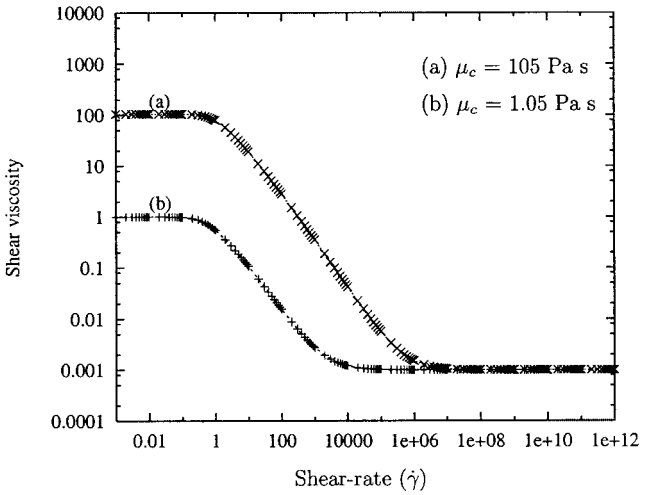


Figure 2. EPTT(0.25) shear viscosity (Pa s), $\mu_s(\dot{\gamma})$; $\mu_1/\mu_c \leqslant 0.999$, $\mu_2/\mu_c \leqslant 0.001$ and $\lambda_1 = 1$.

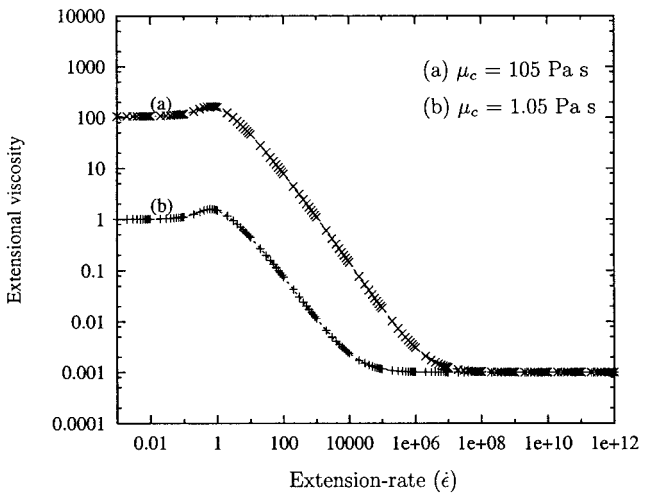


Figure 3. EPTT(0.25) elongational viscosity (Pa s), $\mu_e(\dot{\varepsilon})$; $\mu_1/\mu_c = 0.999$, $\mu_2/\mu_c = 0.001$ and $\lambda_1 = 1$.

stirrer variations are considered: one with a horizontal half-stirrer (E-H1S), and a second, with a vertical half-stirrer (E-V1S).

Numerical solutions are sought for Newtonian, generalized Newtonian (inelastic) and viscoelastic fluids. For the non-Newtonian fluids, shear-thinning is introduced via Carreau (inelastic) and exponential Phan-Thien/Tanner (viscoelastic) models. At a unit value of *We*, the Phan-Thien/Tanner model with a material parameter of $\varepsilon = 0.25$, displays slight strain-hardening at strain-rates O(1) and subsequently strain-softens. With respect to rheological behaviour at different Weissenberg number ($We$) values, shear viscosity ($\mu_s$) and extensional viscosity ($\mu_e$)

 

linearly shift in functional response, so that the same sort of trends are noted, but arise earlier in the deformation-rate ranges.

To complete the problem specification, appropriate initial and boundary conditions are required. Simulations commence from quiescent initial conditions. Boundary conditions are no-slip on solid surfaces, so that the velocity vanishes on the stirrer, whilst at the outer rotating vessel, $v_r = 0$ and $v_\theta = 1$ unit. The pressure vanishes at the vessel wall. For these closed streamlines viscoelastic flows, stress is unspecified at both stirrer and vessel wall.

In this study, due to the nature of the flow problems, the coordinate reference frame is taken as a two-dimensional cylindrical polar system. Numerical results are presented through contour plots of stream-function, pressure, shear-rate, local rate-of work done and the components of stress. Other solution fields of interest are shear-rate, localised rate-of-work and global power are define as

Shear-rate:

$$\dot{\gamma} = \sqrt{2I_2}$$

Local rate-of-work done:

$$\dot{w} = T_e : \nabla \mathbf{u} = \dot{w}_\mu + \dot{w}_\tau$$

Power:

$$\dot{P}_w(t) = \dot{P}_\mu + \dot{P}_\tau = \int_\Omega \dot{w}(\mathbf{x}, t)\, \mathrm{d}\Omega$$

Here, $I_2$ is the second invariant of the rate-of-deformation tensor, $\dot{w}_\mu$ and $\dot{w}_\tau$ are the viscous and elastic contributions of the local rate-of-work done, respectively. $\dot{P}_\mu$ and $\dot{P}_\tau$ are the independent viscous and elastic contributions to power. The total work done upon the system over a time period [0, T], may be defined from the time integral of $\dot{P}_w(t)$.

There are three non-dimensional group numbers relevant here: Reynolds number, $Re = v^{-1}VR$, where kinematic viscosity $v = \mu_c \rho^{-1}$; Weissenberg number, $We = \lambda_1 VR^{-1}$; and Elasticity number, $E = We\, Re^{-1} = \lambda_1 vR^{-2}$. The elasticity number itself interrelates both $Re$ and $We$, so that a level of elasticity may be established for a single set of material parameters, independent of reference velocity scale (or flowrate). The characteristic velocity $V$ is taken to be the speed of the vessel typically 50 rpm, the characteristic length scale is the diameter, 2R, of the stirrer and the characteristic viscosity $\mu_c$ is the zero-shear viscosity.

Appropriate scaling in each variable takes the form: $p = p^*(V\mu_c/R)$, $\dot{\gamma} = \dot{\gamma}^*(V/R)$, $\dot{W} = \dot{W}^*(\mu_c V^2/R^2)$ and $\tau = \tau^* \mu_c (V/R)$. At a characteristic rotational speed 50 rpm and zero-shear viscosity of 105 Pa s, scaling yields dimensional variables $p = 2444\, p^*$, $\dot{\gamma} = 23.28\dot{\gamma}^*$, $\dot{W} = 56894 W^*$ and $\tau = 2444\tau^*$, with shear-rates $O(10^2)s^{-1}$.

## 4. PARALLEL NUMERICAL METHOD

To compute numerical solutions in primary variables of velocity, pressure and stress, we follow Equations (1)–(8). Here, this involves a parallelized time-marching finite element algorithm. This algorithm follows a so-called fractional-staged semi-implicit Taylor–Galerkin/pressure-correction scheme, par-TGPC [3, 5, 10, 11]. In this algorithm temporal domain discretization is achieved adopting a Taylor series expansion in time, prior to spatial discretization.

 

A pressure-correction operator-split is used to construct a second-order time-stepping scheme [17, 18]. Spatial discretization is achieved via Galerkin approximation for the momentum and streamline-upwinding-Petrov–Galerkin (SUPG) approximation for the stress constitutive equations [19–21]. The finite element basis functions employed in this study are quadratic for velocities and stress ($\phi_i(\mathbf{x})$), and linear for pressure ($\phi_i(\mathbf{x})$). Galerkin integrals are evaluated by a seven-point Gauss quadrature rule. The interpolation takes the form $\mathbf{U}(\mathbf{x}, t_n) = \mathbf{U}_i^n \phi_i(\mathbf{x})$; $P(\mathbf{x}, t_n) = U_i^n \psi_k(\mathbf{x})$; $\tau(\mathbf{x}, t_n) = \mathbf{T}_i^n \phi_i(\mathbf{x})$; from which the fully discrete system emerges in vector–matrix form:

*Stage* 1a:

$$\left[\frac{2Re\mathbf{M}}{\Delta t} + \frac{\mathbf{S}}{2}\right](\mathbf{U}^{n+(1/2)} - \mathbf{U}^n) = \{\mathbf{L}^\dagger P - \mathbf{S}\mathbf{U} - \mathbf{D}^\dagger \mathbf{T} - Re\mathbf{N}(\mathbf{U})\mathbf{U}\}^n$$

$$\frac{2We}{\Delta t}\mathbf{M}(\mathbf{T}^{n+(1/2)} - \mathbf{T}^n) = [2\mu_1 \mathbf{D}\mathbf{V} - \mathbf{M}\mathbf{T}]^n - We\{\mathbf{N}(\mathbf{V})\mathbf{T} + \mathbf{F}(\mathbf{T})\mathbf{V}\}^n$$

*Stage* 1b:

$$\left[\frac{Re\mathbf{M}}{\Delta t} + \frac{\mathbf{S}}{2}\right](\mathbf{U}^* - \mathbf{U}^n) = \{\mathbf{L}^\dagger P - \mathbf{S}\mathbf{U}\}^n - \{\mathbf{D}^\dagger \mathbf{T} - Re\mathbf{N}(\mathbf{U})\mathbf{U}\}^{n+(1/2)}$$

$$\frac{We}{\Delta t}\mathbf{M}(\mathbf{T}^{n+1} - \mathbf{T}^n) = [2\mu_1 \mathbf{D}\mathbf{V} - \mathbf{M}\mathbf{T}]^{n+(1/2)} - We\{\mathbf{N}(\mathbf{V})\mathbf{T} + \mathbf{F}(\mathbf{T})\mathbf{V}\}^{n+(1/2)}$$

*Stage* 2:

$$\theta\mathbf{K}(P^{n+1} - P^n) = \frac{1}{\Delta t}\mathbf{L}\mathbf{V}^*$$

*Stage* 3:

$$\frac{1}{\Delta t}\mathbf{M}(\mathbf{V}^{n+1} - \mathbf{V}^*) = -\theta\mathbf{L}^\dagger(P^{n+1} - P^n)$$

Utilizing implied inner product notation $\langle\,\rangle$ for domain integrals, the above system involves matrices of the form:

Mass matrix; $\mathbf{M} = \langle \phi_i \phi_j \rangle$,

Pressure gradient matrix; $\mathbf{L} = (L_r, L_\theta) = \left\langle \left( \frac{\partial \phi_i}{\partial r}\psi_k, \frac{1}{r}\frac{\partial \psi_i}{\partial_r \theta}\psi_k \right) \right\rangle$,

Gradient matrix; $\mathbf{D} = (D_r, D_\theta, D) = \left\langle \left( \frac{\partial \phi_i}{\partial r}\phi_i, \frac{1}{r}\frac{\partial \phi_i}{\partial \theta}\phi_i, \frac{1}{r}\phi_i\phi_j \right) \right\rangle$,

Stiffness matrix; $\mathbf{K} = \left\langle \frac{\partial \psi_1}{\partial r}\frac{\partial \psi_k}{\partial r} + \frac{1}{r^2}\frac{\partial \psi_1}{\partial \theta}\frac{\partial \psi_k}{\partial \theta} \right\rangle$,

Non-linear advection matrices;

$$\mathbf{N}(\mathbf{U}) = (N(\mathbf{U}), N_1)) = \left\langle \left( \phi_i \left( \phi_l \mathbf{V}_r^l \frac{\partial \phi_j}{\partial r} + \frac{1}{rl}\phi_l \mathbf{V}_\theta^l \frac{\partial \phi_j}{\partial \theta}, \phi_i \phi_l \mathbf{V}_\theta^l \phi_j \right) \right) \right\rangle$$

Non-linear elastic matrices; $\mathbf{F}(\mathbf{T}) = (F_1, F_2, F_3, F_4, F_5)$

 

where

$$\mathbf{F}_1 = \left\langle \phi_i \left( \phi_l T^l_{rr} \frac{\partial \phi_j}{\partial r} + \frac{1}{r} \phi_l T^l_{r\theta} \frac{\partial \phi_j}{\partial \theta} \right) \right\rangle, \quad \mathbf{F}_2 = \left\langle \phi_i \left( \phi_l T^l_{r\theta} \frac{\partial \phi_j}{\partial r} + \frac{1}{r} \phi_l T^l_{\theta\theta} \frac{\partial \phi_j}{\partial \theta} \right) \right\rangle$$

$$\mathbf{F}_3 = \left\langle \phi_i \frac{1}{r} \phi_l T^l_{rr} \phi_j \right\rangle, \quad \mathbf{F}_4 = \left\langle \phi_i \frac{1}{r} \phi_l T^l_{r\theta} \phi_j \right\rangle, \quad \mathbf{F}_5 = \left\langle \phi_i \frac{1}{r} \phi_l T^l_{\theta\theta} \phi_j \right\rangle$$

and diffusion matrices; $\mathbf{S} = (\mathbf{S}_{rr}, \mathbf{S}_{r\theta}, \mathbf{S}_{\theta\theta})$, where

$$\mathbf{S}_{rr} = \mu_2 \left\langle \left( 2 \frac{\partial \phi_i}{\partial r} \frac{\partial \phi_j}{\partial r} + \frac{2}{r^2} \phi_i \phi_j + \frac{1}{r^2} \frac{\partial \phi_i}{\partial \theta} \frac{\partial \phi_j}{\partial \theta} \right) \right\rangle$$

$$\mathbf{S}_{r\theta} = \mu_2 \left\langle \left( \frac{1}{r} \frac{\partial \phi_i}{\partial \theta} \frac{\partial \phi_j}{\partial r} + \frac{2}{r^2} \phi_i \frac{\partial \phi_j}{\partial \theta} - \frac{1}{r^2} \frac{\partial \phi_i}{\partial \theta} \phi_j \right) \right\rangle$$

$$\mathbf{S}_{\theta\theta} = \mu_2 \left\langle \left( \frac{\partial \phi_i}{\partial r} \frac{\partial \phi_j}{\partial r} + \frac{1}{r^2} \phi_i \phi_j - \frac{1}{r^2} \phi_i \frac{\partial \phi_j}{\partial r} - \frac{1}{r} \frac{\partial \phi_i}{\partial r} \phi_j + \frac{2}{r^2} \frac{\partial \phi_i}{\partial \theta} \frac{\partial \phi_j}{\partial \theta} \right) \right\rangle$$

The time-step, $\Delta t$, is taken as $10^{-2}$, so as to satisfy a local courant condition constraint [18–21]. The implicit splitting of pressure terms in the pressure-correction leads to the factor $\theta$, and a second-order scheme if taken as $\frac{1}{2}$. In addition, the Crank–Nicolson splitting of diffusion terms at stage-1, incorporates the implicit diffusion contribution to the left-hand side of the equation.

### *4.1. Parallelization strategy*

The semi-implicit time-stepping par-TGPC algorithm is implemented with recourse to the message passing protocol, PVM. Each of the three individual fractional-stage phases of the algorithm is parallelized within a single time-step loop. This implies operations of gather and scatter of data, pre- and post-each phase, respectively. We relate such operations, through PVM *send* and *receive* communication commands, with message passing between master and slave processors. This is an important issue to ensure protocol integrity, correct system configuration and network communication. The domain is partitioned into several sub-domains and the combined, problem is segregated into associated sub-problems, each relating to an individual sub-domain. The system of equations, at stages one and three, are solved by an iterative Jacobi technique. At stage two, a Poisson equation, for the temporal difference of pressure is solved by a direct Choleski method. Within each time-step loop, all fractional-stages are parallelized independently. As this algorithm is dominated by construction of right-hand side vectors, through element loops and iterative compute phases, time consumption is theoretically linear in degrees-of-freedom per time step. Speed-up, via parallelism, should also reflect this property over the processors, provided communication overhead is minimal compared with process calculation time. Limitations due to large problem size may be significantly reduced with distribution of memory resource for each subproblem. For efficiency, the direct Choleski solution process necessitates optimised node numbering and bandwidth reduction. A general-

 

ization of Sloan's algorithm [22] over multiple domains is used to achieve such bandwidth reduction through reordering of node numbers.

Only the pressure equation step is solved through a direct procedure (Choleski), involving the explicit parallel construction and solution of a matrix problem. It is upon this basis that the present parallel performance characteristics are achieved. A comprehensive description on the parallelization of par-TGPC and the algebraic solution procedures is give in Reference [11]. Briefly, both direct and iterative procedures necessitate an assembly and solution phase, involving finite element loop construction of right-hand side vectors and matrix components. For the Choleski procedure, invoked for pressure, the matrix components must be stored. Fortunately, this is manageable even for large problems, as the pressure variable is of scalar form over the domain.

The iterative solution phase is nodally based. Each sub-problem on a slave processor, first computes for the boundary (interfacing) nodes, so that their result may be communicated to the master processor directly, whilst the computation for interior sub-domain nodes is completed. This enables effective masking of communication. The combined domain contributions for the interfacing nodes are processed by the master processor, which also controls system synchronization and processor intercommunication. The parallel finite element Jacobi iteration may be expressed in concise notational form for a domain partitioned into $n$ sub-domains, as

$$\text{par}\uparrow\downarrow \begin{bmatrix} \mathbf{X}_{P_1} \\ \cdots \\ \mathbf{X}_{P_2} \\ \cdots \\ \mathbf{X}_{P_3} \\ \cdots \\ \vdots \\ \cdots \\ \mathbf{X}_{P_n} \end{bmatrix}_{\text{nodes}}^{r+1} = (I - \omega \mathbf{M}_d^{-1} \mathbf{M}_{fe}) \begin{bmatrix} \mathbf{X}_{P_1} \\ \cdots \\ \mathbf{X}_{P_2} \\ \cdots \\ \mathbf{X}_{P_3} \\ \cdots \\ \vdots \\ \cdots \\ \mathbf{X}_{P_n} \end{bmatrix}_{\text{nodes}}^{r+1} + \omega \mathbf{M}_d^{-1} [\mathbf{b}]_{\text{nodes}}$$

The notation implies an iteration number $r$, acceleration factor $\omega$, right-hand side vector $\mathbf{b}$, iteration sub-domain vector $\mathbf{X}_{P_i}$, system mass matrix $\mathbf{M}_{fe}$ and diagonal matrix $\mathbf{M}_d$. Using boolean transformation element matrices $\mathbf{L}_e$ and element mass matrices $\mathbf{M}_e^{fe}$, system matrices can be represented in the form

$$\mathbf{M}_{fe} = \sum_{elt} \mathbf{L}_e^T \mathbf{M}_e^{fe} \mathbf{L}_e; \quad \mathbf{M}_d = f_{\text{diag}}(\mathbf{M}_{fe})$$

A single iteration sweep of this type will maintain integrity levels of the data re-synchronisation. Care, likewise, must be taken with respect to consistent solution increment tolerance calculations across individual slave and master processors. We recall that the master processor must gather the iterative contributions to interfacing nodes, that normally straddle more than one sub-domain.

 

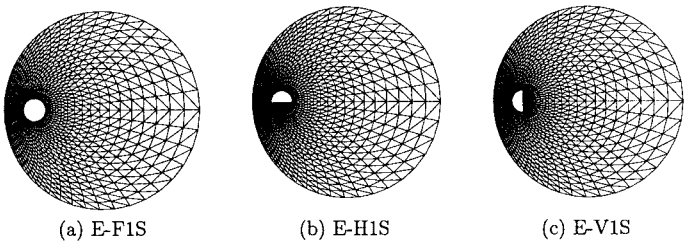


Figure 4. Finite element meshes: Mesh-M2 series.

The parallel direct solution phase adopts a Schur-complement approach. This introduces a parallel herring-bone structure for the Choleski system matrix which may be represented as

$$\text{par}\uparrow\downarrow \left[\begin{array}{cccccc|c} [P_1] & & & & & & [MP_1] \\ & [P_2] & & & & & [MP_2] \\ & & [P_3] & & & & [MP_3] \\ & & & \ddots & & & \vdots \\ & & & & \ddots & & \vdots \\ & & & & & [P_n] & [MP_n] \\ \hline [P_1M] & [P_2M] & [P_3M] & & & [P_nM] & [M] \end{array}\right]$$

with $[P_i]$ the matrix for the sub-domain problem for the interior of sub-domain $i$, $[P_i\mathbf{M}]$, the matrix contribution of interior sub-domain $i$ to the boundary-node problem, and $[\mathbf{M}]$ that for the boundary-nodes. Each interior sub-domain problem may be solved in parallel with all others. Finally, the interfacing-node matrix problem is solved, for which all available processors may be pooled. To date, the size of the interfacing-node matrix problem has been such that it was only necessary to use a single processor (the master) for this task. In such a manner, large-scale problems, typically of three-dimensional or viscoelastic form [11] become tractable.

### *4.2. Meshing and domain decomposition*

Finite element meshes for these problems are displayed in Figure 4. For each domain, we have generated three different meshes to check for mesh convergence. This has been managed so that maximum differences are within one percent between solutions on any two consecutively refined meshes. Table I records the detailed statistics for the meshes employed.

The domain of interest is decomposed into a number of subdomains, according to available resources. In this study, uniform load distribution is ensured using a recursive spectral bisection method [23]. As the recursive spectral bisection method basically supports partitioning in powers of two, a partitioning method is employed for six and twelve subdomains using information from eight and sixteen subdomains splits, as gathered from RSB. The various sub-domains generated in this manner are illustrated in Figure 5 for 2, 4, 6, 8, 12 and

 

Table I. Finite element mesh data.

| Meshes | Elements | Nodes | DOF(N) | DOF(V) |
|---|---|---|---|---|
| E-F1S | | | | |
| M1 | 1536 | 3168 | 7152 | 16656 |
| M2 | 2560 | 5248 | 11840 | 27584 |
| M3 | 3840 | 7840 | 17680 | 41200 |
| E-H1S | | | | |
| M1 | 1704 | 3488 | 7868 | 18232 |
| M2 | 2784 | 5672 | 12788 | 29804 |
| M3 | 4200 | 8530 | 19225 | 44815 |
| E-V1S | | | | |
| M1 | 1704 | 3488 | 7868 | 18232 |
| M2 | 2784 | 5672 | 12788 | 29804 |
| M3 | 4200 | 8530 | 19225 | 44815 |

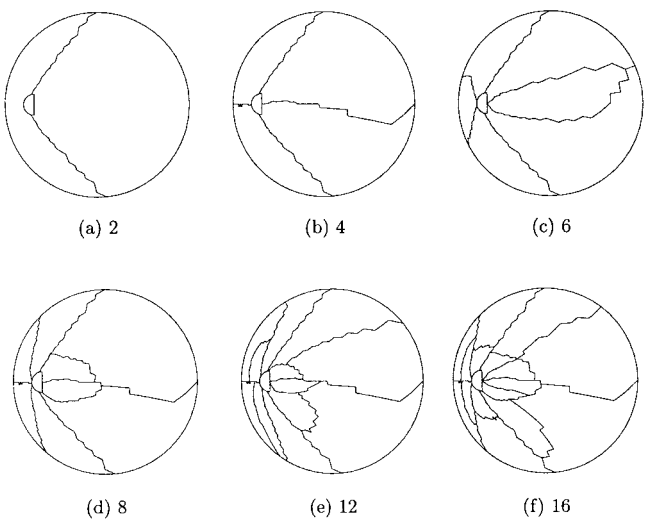


Figure 5. Typical domain partitions.

16 subdomains. For six and twelve subdomains, a uniform load distribution is not strictly extracted. With an increasing number of subdomains, interfacing nodes ($\mathrm{In_n}$) increase (as does communication cost), whilst the number of elements, nodes ($N_\mathrm{n}$) and degrees-of-freedom per subdomain decreases. Table II, presents the number of elements, nodes and DOF per subdomain, the number of interfacing nodes (master/slave) and ratio of subdomain nodes to interfacing nodes ($G_\mathrm{n} = N_\mathrm{n} : \mathrm{In_n}$).

 

Table II. Domain decomposition data for E-V1S; mesh-M3 series.

| Domains | Elements/ subdomain | Nodes/ subdomain | Interface nodes | | DOF(N) | DOF(V) | $C_n$ | |
|---|---|---|---|---|---|---|---|---|
| | | | Slave | Master | | | Slave (%) | Master (%) |
| 1 | 4200 | 8530 | 0 | 0 | 19225 | 44815 | — | — |
| 2 | 2100 | 4314 | 98 | 98 | 9760 | 22702 | 2.3 | 2.3 |
| 4 | 1050 | 2186 | 113 | 216 | 4938 | 11496 | 5.2 | 9.9 |
| 6 | 700 | 1475 | 112 | 318 | 3375 | 7800 | 7.6 | 21.5 |
| 8 | 525 | 1115 | 109 | 393 | 2513 | 5858 | 9.8 | 35.2 |
| 12 | 350 | 758 | 108 | 545 | 1728 | 4002 | 14.2 | 71.9 |
| 16 | 262 | 567 | 111 | 620 | 1275 | 2976 | 19.6 | 109 |

## 5. SOLUTION CONTINUATION PROCEDURE

In order to compute viscoelastic solutions to the extreme levels of material parameters involved here, a detailed and selective path of numerical continuation must be adopted. It is a technically challenging problem to accomplish this task, as numerical stability is extremely restrictive in this respect. It is noteworthy, that all current numerical algorithms in vogue today meet such barriers and the accomplishments therein are somewhat limited. The two significant parameter spaces we explore, that fall within this category, are high Weissenberg number (large $\lambda_1$) and predominant solute viscosity factor ($\mu_1^* = (\mu_1/\mu_c)$. The fact that the EPTT model can support relatively high $We$ (up to $O(10^2)$ and large $\mu_1$ (approaching unity) solutions has been demonstrated elsewhere, under industrial level requirements [24–26]. Reaching such high elasticity levels is an open and current research topic (see review articles, [27–30]). The issue surrounding the viscosity split level is somewhat related to the foregoing, in that it governs the amount of solvent stress apportioned to the system (hence, governs departure from Maxwellian specification), and this provides a level of stability to the problem.

Our target is to compute solutions to $We = 13$ ($\lambda_1 = 0.56$ s and $(\mu_2/\mu_1) = \frac{1}{999}$) for the EPTT(0.25) model at any particular $Re$ level (say, $Re = 0.08$ with $\mu_c = 105$ Pa s). To achieve this, we adopt a number of different continuation paths. First, we establish a coupled viscoelastic solution, commencing from an initial state of rest, for a relatively low level of Weissenberg number ($We \leqslant 4.6$) and viscosity split of $\frac{1}{2}$. From this solution, we are able to compute coupled solutions and decrease the viscosity split to $\frac{3}{7}$. To elevate the level of elasticity to $We = 13$, it is necessary to subsequently decouple the solution procedure and freeze the velocity field, hence computing a stress field [31]. Such a stress solution may then be recycled to reestablish a consistent kinematic field. The final stage of the process is to compute a stress solution at a level of $\frac{1}{999}$. This most severe level is accomplished again through a decoupled step, as above.

The precise choice of values is not so significant here, but the phased continuation is crucial. Clearly, the above procedure is a tortuous path, but one that is pragmatic and absolutely essential to make headway in this challenging domain. We are careful to point out that, we invoke a coupled viscoelastic solution (including kinematics), in an attempt to remain close to the desired ultimate solution. That is, in place of a totally decoupled approach frequently cited in the literature [32], in which inelastic kinematics may be invoked instead.

 

## 6. NUMERICAL RESULTS

The numerical results are investigated from two distinct points of view: through geometry adjustment (E-F1S, E-H1S and E-V1S) and change of fluid (Newtonian, inelastic and viscoelastic). This leads to analysis with respect to increasing viscosity levels (decrease of Reynolds number), influence of different rheological behaviour (viscous to shear-thinning, with and without memory, increasing relaxation time) and comparison of flow structure variation across problem instances (reflecting localised rate-of-work and global power consumption). The predicted solutions are displayed through contours plots of streamlines, shear-rate, rate-of-work done, pressure and stress. Pressure and stress patterns are plotted with eleven contours, from the minimum to maximum value, over a fixed range. Streamlines are plotted in two regions: first from the vessel wall to the stirrer perimeter, $0.0 \leqslant \Psi \leqslant 2.95$ at increments of 0.5 units, and second, from the stirrer to the centre of the recirculation, $3.05 \leqslant \Psi \leqslant \Psi_{\max}$ at increments of 0.2 units. Comparative diagnostics may be derived accordingly.

Various increasing levels of zero-shear viscosities $\mu_c$ (characteristic) are considered, from which Reynolds number is computed, as defined above. For Reynolds numbers of $Re = 8.0$, 0.8 and 0.08, the corresponding zero-shear viscosities are $\mu_c = 1.05$, 10.5 and 105.0 Pa s. Of these levels, a range of material properties is covered from those for model fluids, to model dough, to actual dough, respectively.

### 6.1. *Flow patterns with increasing inertia*

The effect of increasing Reynolds number upon streamline patterns is represented in contour plots for all three problems: full stirrer (E-F1S, Figure 6), horizontal half-stirrer (E-H1S,

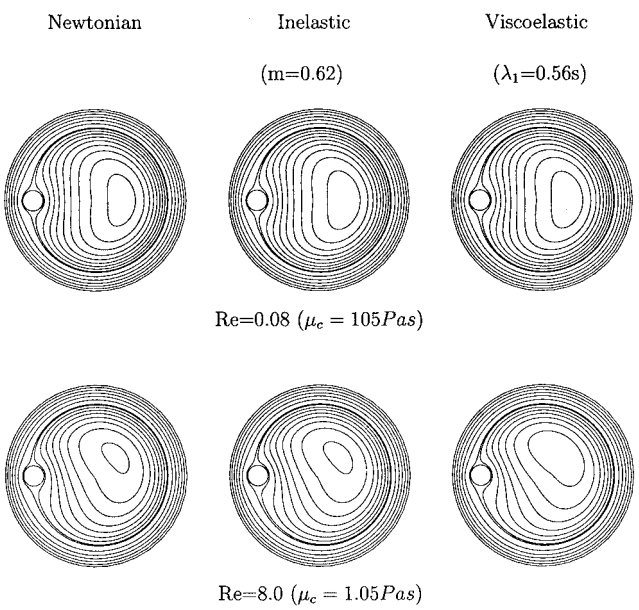


Figure 6. Streamfunction: E-F1S.

 

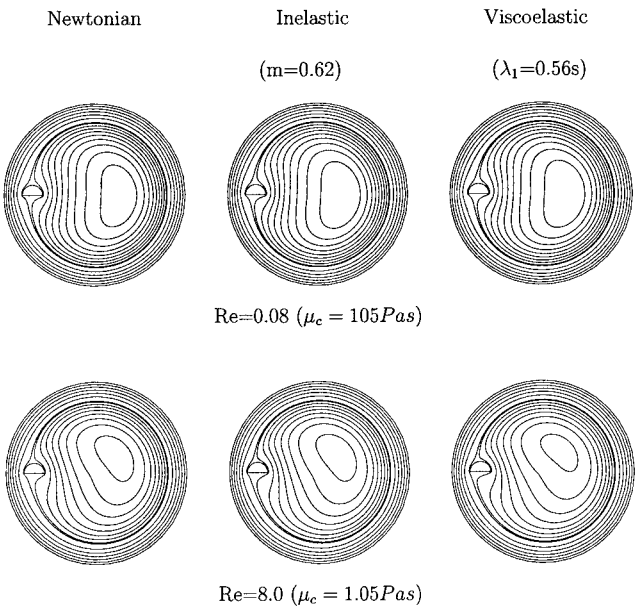


Figure 7. Streamfunction: E-H1S.

Figure 7) and vertical half-stirrer (E-V1S, Figure 8). Such data are provided at $Re = 0.08$ and 8 for Newtonian, inelastic and viscoelastic EPTT(0.25) fluids. At a low level of inertia, $Re = 0.08$, and for all problem instances, an intense recirculating region forms in the centre of the vessel, parallel to the stirrer and symmetrically intersecting the diameter that passes through the centres of the vessel and stirrer. Flow structure remains unaffected as $Re$ rises to values of O(1); hence we suppress this data. However, upon increasing Reynolds number up to eight, so O(10), inertia takes hold and the recirculation region shifts towards the upper-half plane, vortex intensity wanes and the vortex eye is pushed towards the vessel wall. The flow becomes asymmetric as a consequence of the shift in vortex centre. Comparing inelastic and Newtonian flow patterns, it is apparent that shear-thinning does not alter either the flow structure or the shift in recirculating eddy position. This is true irrespective of the level of $Re$. The introduction of elasticity does not alter the above findings at $Re = 0.08$. In contrast, at $Re = 8$ and for viscoelastic over viscous fluids, there is a more exaggerated twist of the asymmetric vortex pattern in the direction of the vessel motion. Elasticity is found to promote the shift of vortex centre towards the vessel wall and reduces vortex intensity. Overall, fluid memory and shear-thinning effects have only a mild influence on these streamline patterns. It is the inertial influence that dominates.

We may contrast the flow patterns across all three geometry variants: E-F1S, E-H1S and E-V1S. For E-H1S, in contrast to E-F1S, the flow manifests more dramatic compression and expansion around both sides of the stirrer. For viscoelastic fluids, this abrupt change in flow structure plays an important role (see on). In the E-V1S case compared to E-F1S, the flow circumvents the stirrer more smoothly on the side towards the vessel centre, whilst on the counterside of the stirrer, the flow structure emulates that of E-F1S.

 

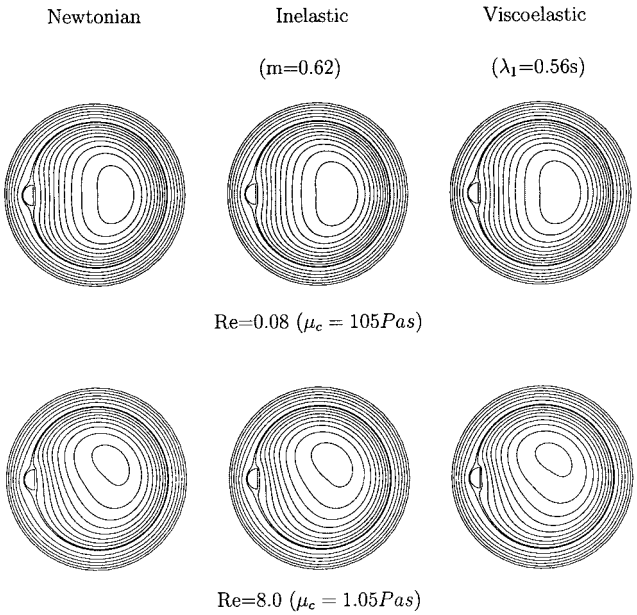


Figure 8. Streamfunction: E-V1S.

### 6.2. *Field data, E-F1S*

For the inelastic (fluid-1b) simulations and all three geometries, we first plot pressure, shear-rate and local rate-of-work. Results at $Re = 0.08$ appear in Figure 9, whilst Figure 10 covers data for the higher inertial level of $Re = 8$. For E-F1S and E-V1S domains at $Re = 0.08$, symmetric pressure isobars appear with equal magnitude in non-dimensional positive and negative extrema on the two sides (upper and lower) of the stirrer in the narrow-gap. The extrema for E-V1S correspond to the sharp tips of the stirrer and double the values of those for E-F1S. Whilst for E-H1S case, asymmetric contours are observed, with positive maximum on the top of the stirrer (as for E-F1S, of same order), and negative minimum at the outer stirrer tip (near the narrow-gap, of equal order to E-V1S), see Table III.

Similar symmetry arguments apply across the geometry variants in variables of shear-rate and rate-of-work done. Extrema in shear-rate and rate-of-work are replicated for E-F1S and E-V1S. In contrast, the E-H1S case generates increase in shear-rate of fifty percent and rate-of-work doubles. These extrema always remain on the stirrer at the narrowest part of the gap between stirrer and vessel wall. For E-H1S, this location corresponds to the sharp tip of the stirrer.

As we increase inertia to $Re = 8$, and contrast Figures 9–10, asymmetrical flow structure is observed in all variables and across all geometries. In non-dimensional terms above $Re = 0.08$ (noting scale differences), there is increase in pressure-differential, shear-rates rise by as much as twenty-five percent and by even more in rate-of-work. For the Newtonian (fluid-1a) results (not shown here), as compared to the equivalent inelastic fluid-1b, shear-rates decrease, whilst pressure differential and localized rate-of-work increase. For both types of fluid, the extrema of shear-rate and rate-of-work, along with power and pressure differential, are tabulated for completeness in Table III at $Re = 0.08$.

 

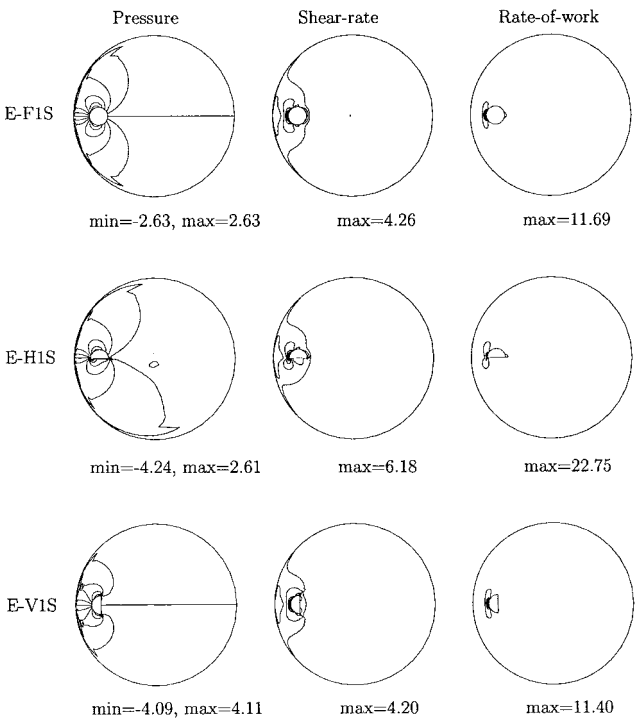


Figure 9. Field plots: inelastic fluid-1b, $Re = 0.08$ ($\mu_c = 105$ Pa s).

Corresponding field kinematic data for viscoelastic fluid-2 at $Re = 0.08$ are presented in Figure 11 and stress components are displayed in Figure 12. In contrast to viscous fluids-1b, the contours of pressure, shear-rate and local rate-of-work are now asymmetric, even at this low level of inertia. Pressure differentials are generally lowered, and similar balance in extrema is noted to those for fluid-1b in E-F1S and E-H1S flows. However, the position for E-V1S differs from fluid-1b, in that positive maxima exceed negative minima by about fifty percent. As in Table IV, trends in maxima of shear-rate follow the inelastic fluid-1b, noting that greater shear-thinning is associated with the EPTT(0.25) fluid-2. Local rate-of-work maxima are now an order of magnitude smaller than those for viscous fluids-1, and the non-symmetric stirrer cases provide double the values of E-F1S. If anything, there is slightly larger rate-of-work done in the E-H1S above E-V1S case at this inertial level (see Tables IV and V for contrast in $Re$). Another feature is the wider dispersal of shear-rate and rate-of-work for fluid-2 above fluid-1. As a consequence, we attribute this largely to fluid memory effects.

In Figure 12, we contrast field data on the three elastic stress components across the three mixer designs. The hoop stress tends to dominate the other components (azimuthal stretching), displaying the more prominent and extended wake region beyond the stirrer, in a zone close to the vessel wall occupied by flow lines that encounter the stirrer. Also, radial stress is non-negligible (radial stretching). Accounting for differentials (max-min) of stress, we are able to discern that E-V1S results closely resemble those of E-F1S. If anything, there is only minor rebalancing between hoop and shear stress, from E-F1S to E-V1S case. The principal point is

 

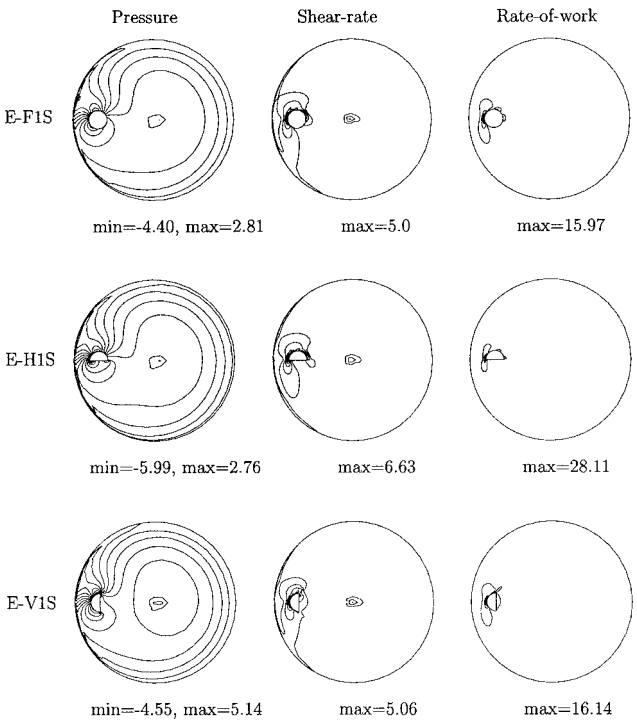


Figure 10. Field plots: inelastic fluid-1b, $Re = 8$ ($\mu_c = 1.05$ Pa s).

Table III. Viscous fluids-1(a, b): shear-rate, local rate-of-work maxima; power; $\beta = 10^{-2}$; $Re = 0.08$ ($\mu_c = 105$ Pa s).

| | Newtonian | | | | | Inelastic | | | | |
|---|---|---|---|---|---|---|---|---|---|---|
| Problem | $\dot{\gamma}$ | $\dot{w}$ | $\dot{P}_w$ | $\Delta P$ | $\beta(\dot{w} : \dot{P}_w)$ | $\dot{\gamma}$ | $\dot{w}$ | $\dot{P}_w$ | $\Delta P$ | $\beta(\dot{w} : \dot{P}_w)$ |
| E-F1S | 3.78 | 12.60 | 1446 | 6.10 | 0.87 | 4.26 | 11.69 | 1244 | 5.26 | 0.94 |
| E-H1S | 5.05 | 25.19 | 1364 | 7.71 | 1.85 | 6.18 | 22.75 | 1173 | 6.85 | 1.94 |
| E-V1S | 3.53 | 12.24 | 1539 | 9.50 | 0.80 | 4.20 | 11.40 | 1339 | 8.21 | 0.85 |

the significant rise from E-F1S to E-H1S flow in both shear and hoop stress differentials. The hoop stress differential doubles, whilst the shear stress differential triples. We observe that both such quantities will contribute to shear and extensional elastic work, as flow lines distort away from an orthogonal circular co-ordinate frame-of-reference. This arises in the vicinity of the stirrer, where stress extrema occur. Radial stress differentials are slightly larger than those of shear stress, in E-F1S and E-V1S geometries, and infact dominate for E-V1S. For the E-H1S flow, the radial stress differential drops to about half that corresponding to shear or hoop stress differential.

 

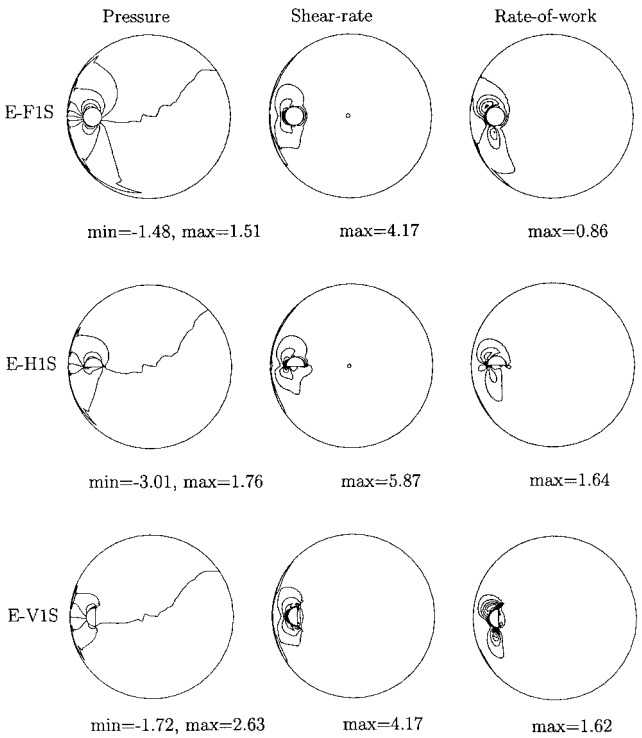


Figure 11. Field plots, viscoelastic fluid-2: $We = 13$ ($\lambda_1 = 0.56$ s), $Re = 0.08$ ($\mu_c = 105$ Pa s).

### 6.3. *Variation with fluids:* $\dot{w}$, $\dot{P}_w$

To make direct comparisons across geometries for individual fluids, with particular reference to localised rate-of-work and global power, we tabulate sampled maxima in Tables III–VII.

*6.3.1. Viscous fluids-1* $(a,b)$. We begin with viscous fluid-1 (Newtonian and inelastic) in Table III, where shear-rate, local rate-of-work done, global power and pressure differential are tabulated for all three problem instances. For the full-stirrer case (E-F1S), maxima in shear-rate increase from Newtonian to inelastic fluids. Maxima in local rate-of-work, global power and pressure differential decrease. Here, the local rate-of-work is dominated by shear viscous influence. This decreasing trend with increase in shear-rate, in local rate-of-work, global power and pressure differential, is also observed in E-H1S and E-V1S problems. For both fluids and the E-H1S instance, in contrast to either E-F1S or E-V1S cases, maxima in shear-rate increase by fifty percent and local rate-of-work doubles. Alternatively, for E-H1S flow, global power on the entire domain, is reduced over the other two cases. This illustrates the more localised concentration of rate-of-work about the narrow-gap stirrer-tip for E-H1S (see Figures 9 and 10). For E-V1S flow, global power and pressure differential are greater than that for E-F1S and E-H1S variants.

Hence, for viscous fluids-1, optimal mixer $\dot{w} : \dot{P}_w$ rating is attributed to E-H1S design, doubling that for the two contender options.

 

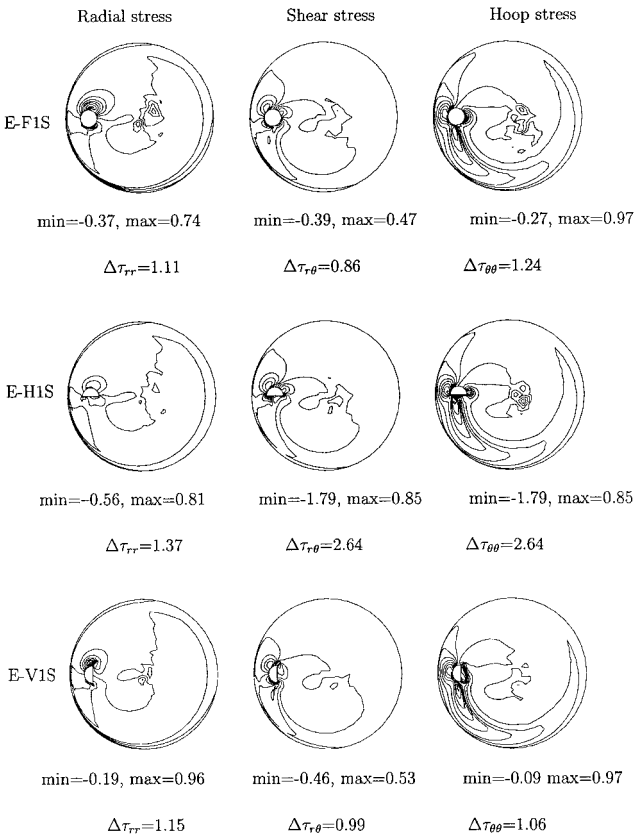


Figure 12. Stress, viscoelastic fluid-2: $We = 13$ ($\lambda_1 = 0.56$ s), $Re = 0.08$ ($\mu_c = 105$ Pa s).

Table IV. Viscoelastic fluid-2: shear-rate, hoop stress, local rate-of-work maxima; power and pressure differential; $\beta = 10^{-2}$; $Re = 0.08(\mu_c = 105$ Pa s), $We = 13$ ($\lambda_1 = 0.56$ s), $E = 162.5$.

| Problem | $\dot{\gamma}$ | $\tau_{\theta\theta}$ | $\dot{w}_\mu$ | $\dot{w}_\tau$ | $\dot{w}$ | $\dot{P}_\mu$ | $\dot{P}_\tau$ | $\dot{P}_w$ | $\Delta P$ | $\beta(\dot{w} : \dot{P}_w)$ |
|---|---|---|---|---|---|---|---|---|---|---|
| E-F1S | 4.17 | 0.97 | 0.02 | 0.84 | 0.86 | 1.73 | 246.5 | 248.2 | 2.99 | 0.35 |
| E-H1S | 5.87 | 0.99 | 0.03 | 1.64 | 1.64 | 1.74 | 260.1 | 261.9 | 4.77 | 0.63 |
| E-V1S | 4.17 | 0.97 | 0.02 | 1.61 | 1.62 | 1.88 | 276.5 | 278.4 | 4.35 | 0.58 |

Table V. Viscoelastic fluid-3: shear-rate, hoop stress, local rate-of-work maxima; power and pressure differential; $\beta = 10^{-2}$; $Re = 8(\mu_c = 10.5$ Pa s), $We = 13$ ($\lambda_1 = 0.56$ s), $E = 1.625$.

| Problem | $\dot{\gamma}$ | $\tau_{\theta\theta}$ | $\dot{w}_\mu$ | $\dot{w}_\tau$ | $\dot{w}$ | $\dot{P}_\mu$ | $\dot{P}_\tau$ | $\dot{P}_w$ | $\Delta P$ | $\beta(\dot{w} : \dot{P}_w)$ |
|---|---|---|---|---|---|---|---|---|---|---|
| E-F1S | 6.09 | 1.05 | 0.04 | 1.55 | 1.59 | 2.68 | 255.4 | 258.1 | 5.25 | 0.62 |
| E-H1S | 7.88 | 1.84 | 0.06 | 3.59 | 3.64 | 2.87 | 466.2 | 469.1 | 7.87 | 0.78 |
| E-V1S | 5.87 | 1.24 | 0.04 | 1.82 | 1.83 | 2.94 | 289.8 | 292.7 | 6.50 | 0.63 |

 

Table VI. Viscoelastic fluids-4(a, b), E-F1S: shear-rate, hoop stress, local rate-of-work maxima; power and pressure differential; $\beta = 10^{-2}$; $Re = 8(\mu_c = 1.05\ \text{Pa s})$, $We = 1.5$ $(\lambda_1 = 0.065\ \text{s})$, $E = 0.1875$.

| $\mu_2 : \mu_1$ | $\dot{\gamma}$ | $\tau_{\theta\theta}$ | $\dot{w}_\mu$ | $\dot{w}_\tau$ | $\dot{w}$ | $\dot{P}_\mu$ | $\dot{P}_\tau$ | $\dot{P}_w$ | $\Delta P$ | $\beta(\dot{w} : \dot{P}_w)$ |
|---|---|---|---|---|---|---|---|---|---|---|
| 1:999 | 8.12 | 5.49 | 0.07 | 11.25 | 11.32 | 0.51 | 164.3 | 164.8 | 4.57 | 6.87 |
| 1:8 | 7.07 | 4.34 | 5.56 | 8.37 | 13.93 | 48.73 | 137.9 | 186.6 | 4.03 | 7.46 |

Table VII. Viscoelastic fluid-2: local rate-of-work maxima; $Re = 0.08(\mu_c = 105$ Pa s), $We = 13(\lambda_1 = 0.56\ \text{s})$, $E = 162.5$.

| | E-F1S | | E-H1S | | E-V1S | | |
|---|---|---|---|---|---|---|---|
| Rate-of-work | Pre-gap Max | Post-gap | Pre-gap | Sub-stirrer Max | Pre-gap | Post-gap | Stirrer-tip Max |
| $\dot{w}_\tau^s$ | 1.31 | −0.50 | 1.49 | 1.33 | 1.33 | −0.33 | 0.93 |
| $\dot{w}_\tau^e$ | −0.47 | 1.13 | −0.37 | 0.38 | −0.48 | 1.03 | 0.68 |
| $\dot{w}_\tau$ | *0.84* | 0.64 | 1.12 | *1.64* | 0.85 | 0.70 | *1.61* |

*6.3.2. Viscoelastic fluid*-2 ($\mu_c = 105\ \text{Pa s}, \lambda_1 = 0.56\ \text{s}$). For viscoelastic simulations, we go further to tabulate additional quantities in Table IV at $Re = 0.08$. Here, we chart maximum hoop stress ($\tau_{\theta\theta}$), and split components of rate-of-work and power, into those due to viscous solvent and elastic solute contributions. For viscoelastic fluid-2, shear-rates are of the same order as in the inelastic case, for all three problems. Here, to mimic realistic doughs, we have employed a relaxation time O(1) for which $E = 162.5$, and a viscosity split, with miniscule solvent and large elastic solute component. The ratio of these fractional viscosities is taken as 1:999. Due to the small solvent presence, maxima in viscous portions of both local rate-of-work and global power are small. Here, the dominant factor is the elastic contribution. Due to fluid memory and excess shear-thinning effects there is consequent reduction in localised rate-of-work and global power, which are about ten and five times lower, respectively, than for the equivalent Newtonian and inelastic fluids. Pressure differential is also smaller, approximately halved. This trend is conveyed across all three problem instances.

For such materials, optimal mixer $\dot{w} : \dot{P}_w$ rating resides with E-H1S design. The reduction to E-V1S design is now only minor, so that both unsymmetric stirrer choices double the rating for E-F1S. Hence, from both a viscous and elastic fluid property viewpoint, the unsymmetric stirrer design is advocated. E-H1S is the optimal selection with respect to maximizing local rate-of-work to power rating.

*6.3.2.1. Split of $\dot{w}_\tau$, fluid*-2. We go further in splitting of $\dot{w}_\tau$, to analyse in a qualitative sense, the segregated components due to shear, $\dot{w}_\tau^s$, and that due to extension, $\dot{w}_\tau^e$. That is, associating extension and shear to be aligned with the orthogonal cylindrical coordinate system. To an engineering approximation, this is largely the case for E-F1S and E-V1S, as flow lines closely approximate circular streamlines in the regions of significance with respect to work, near the vessel wall and by-passing the stirrer. The aim is to establish the relative proportion of $\dot{w}_\tau^e$, as opposed to $\dot{w}_\tau^s$, so that we can identify the enhancement of $\dot{w}_\tau^e$ per unit of power.

 

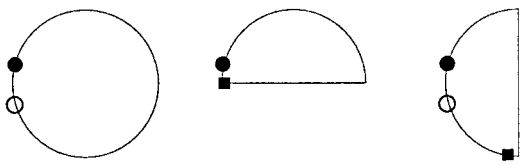

Figure 13. Locations of maxima: $\dot{w}_r$, $\dot{w}_r^s$, $\dot{w}_r^e$.

From this, definitive statements can be made concerning preferential choice re optimality of mixer design. This is an important indicator for mixer design, *viz-a-viz* rheology, to attain work input locally and influence upon material structure. We recall the objective for any specific power rating, is to maximise the elongational rate-of-work component, in preference to that due to shear. In this manner, the link may be established to build-up of desired material structure through kneading.

In Table VII, we record various different sample point values. Concentrating initially upon E-F1S, maxima in elastic-shear $\dot{w}_\tau^s$ corresponds to a pre-narrow-gap surface point on the stirrer. For elastic-extension $\dot{w}_\tau^e$, maxima arise in the post-gap, of similar order to pre-gap $\dot{w}_\tau^s$. Furthermore, at the pre-gap point, the level of $\dot{w}_\tau^e$ is of .equal order to that of post-gap $\dot{w}_\tau^s$. These pre- and post-gap locations are indicated by filled and unfilled circles in Figure 13. We observe that data recorded in Table IV to represent full elastic $\dot{w}_\tau$ equate to pre-gap values. Also, with this equivalence between compression and expansion flow about the stirrer in $\dot{w}_\tau^s$ and $\dot{w}_\tau^e$ maxima, we conclude that the position would be reversed if the motion is translated from the vessel to the stirrer. In contrast, for viscous fluids, $\dot{w}_\mu^e$ peaks at about one half of $\dot{w}_\mu^s$, with such maxima located at similar post- and pre-gap points, as above. Hence, memory fluids can generate significant extensional rate-of-work.

For the unsymmetric stirrer cases, we tabulate the maxima sample point values and the corresponding readings for the same pre- and post-gap locations of E-F1S. For E-V1S flow, similar values are observed at pre- and post-gap points as for E-F1S. This is because stirrer shape is identical within the narrow-gap for these two designs. However, for E-V1S, the maxima arise elsewhere, near the sharp downward-pointing tip of the stirrer within the narrow-gap (see Table IV and Figure 13, where a filled square symbol represents the overall maxima). For E-H1S, pre-gap sample values are as above for E-F1S; maxima arise under the stirrer close to the tip nearest the narrow-gap. This case gives rise to the largest $\dot{w}_\tau$. Due to the complex local orientation of flow lines with the E-H1S geometry, it is difficult to isolate shear and extensional components of work in any meaningful way. To some degree, projected quantities of $\dot{w}_\tau^s$ and $\dot{w}_\tau^e$ at the sub-stirrer point each have mixtures of shear and extensional components. Hence, for E-H1S, only $\dot{w}_\tau$ data should be considered. Nevertheless, splitting of work components does aid in appreciation of the distribution of these localized maxima, associated with the different forms of work.

*6.3.3. Viscoelastic fluid*-3 ($\mu_c = 1.05$ Pa s, $\lambda_1 = 0.56$ s). At $Re = 8$ and $E = 1.625$ in Table V, i.e. model fluids, we record the corresponding values for the same set of variables as in Table IV. Here, the characteristic viscosity is of order one hundred less than for the former viscoelastic fluid-2 (above). In real terms, once scaling is applied, the physical stresses and therefore other qualities that follow suit, are greatly reduced over those for viscoelastic fluid-2.

 

Bearing this point in mind it is instructive to gather inference in the non-dimensional context, from Tables IV–V, as we elevate inertia from $Re = 0.08$–8. Maxima in shear-rate, hoop stress, local rate-of-work, and pressure differential and global power, rise for each problem instance. For E-H1S and E-F1S, shear-rates rise by about fifty percent and this position is reflected in doubling of the local rate-of-work. For E-H1S with increasing $Re$, the maxima in $\dot{w}_\tau$, now switches to above the stirrer. $\dot{w}_\tau$ under the stirrer reduces by twenty-five percent from that at $Re = 0.08$. Adjustment for E-V1S, is far less dramatic. Such factor shifts are barely felt through the global power-rating, in either E-F1S or E-V1S, noting that this (or torque equivalent) is the conventional calibration mechanism. Therefore, it is important to note such insensitivity. However for E-H1S, the power practically doubles above that for fluid-2.

Hence, comparing data directly within Table V at $Re = 8$, the E-H1S instance stands out most prominently. Over other geometries, shear-rate is magnified, extensional hoop stress is doubled, as is the elastic rate-of-work component and total $\dot{w}$. The power also approximately doubles. Oncemore, E-H1S is the optimal design choice on a $\dot{w} : \dot{P}_w$ rating basis and this preference is now quite markedly established.

*6.3.4. Viscoelastic fluids*-4 ($\mu_c = 1.05$ Pa s, $\lambda_1 = 0.065$ s). For the single geometry option E-F1S, we proceed in Table VI to cross-check at $Re = 8$ ($\mu_c = 1.05$ Pa s) on two counts. First, against Table V data, with reduction in elasticity to $E = 0.1875$ ($\lambda_1 = 0.065$ s). That is maintaining the same choice of minimal solvent stress component ($\mu_2/\mu_1 = \frac{1}{999}$, fluid-4a). Hence, memory effects will be apparent. Subsequently, at this lower elasticity level, we also compare data for fluid-4a against the situation with relatively high solvent stress component ($\mu_2/\mu_1 = \frac{1}{8}$, fluid-4b). So here, at equitable fluid memory levels, it is the solvent influence being isolated (see our earlier work [3]).

On the first count, comparing data in Tables V and VI to pinpoint memory effects, so for $\mu_2/\mu_1 = \frac{1}{999}$, $\{\dot{\gamma}, \tau_{\theta\theta}, \dot{w}\}$ maxima are all elevated for fluid-4a over fluid-3. That is, with reduction in elasticity, $\dot{\gamma}$ rises by twenty five percent; $\tau_{\theta\theta}$ increases five-fold and $\dot{w}$ increases by about a factor of ten. Global power declines by about one-half and pressure differential lowers. Significantly, $\dot{w} : \dot{P}_w$ rating increases by one order of magnitude. The contributions to local rate-of-work and global power from viscous stress are clearly negligible, as for fluid-2 and fiuid-3.

When the solvent presence is elevated in contrast, ($\mu_2/\mu_1 = \frac{1}{8}$, fluid-4b), there is little change in total quantities, $\dot{w}$ or $\dot{P}_w$, over fluid-4a. As to be anticipated, there is a switch of some component of the local rate-of-work and power into the solvent portion, but overall the same conclusions apply. This ratifies our earlier findings on $\dot{w}_{\max}$ for fluid-4b, that we explored extensively in Reference [3] for alternative rheology.

### *6.4. Parallel performance*

To establish parallel computing performance in this complex problem setting, we have invoked both homogeneous and heterogeneous distributed computation. A homogeneous network is established using a shared-memory eight-processor Intel Solaris platform, with 16GB memory machine. The heterogeneous network is made up from a mixed four-processor DEC-alpha shared-memory, eight-processor shared-memory and seven single processors distributed-memory Intel clusters. Each of the Intel clusters runs under the Solaris operating system. A public domain PVM3.4.3 version for message passing protocol has been employed to support

 

Table VIII. Speed-up and efficiency on heterogeneous network, E-V1S; Mech-M3.

| Processors | Newtonian | | Viscoelastic | |
|---|---|---|---|---|
| | $S_n$ | $\eta_n$ | $S_n$ | $\eta_n$ |
| 1 | 1.00 | 1.00 | 1.00 | 1.00 |
| 2 | 1.94 | 0.97 | 1.99 | 1.00 |
| 4 | 3.79 | 0.95 | 3.90 | 0.98 |
| 6 | 5.39 | 0.90 | 5.77 | 0.96 |
| 8 | 7.29 | 0.91 | 7.67 | 0.95 |
| 12 | 10.73 | 0.89 | 11.65 | 0.93 |
| 16 | 12.82 | 0.80 | 14.24 | 0.83 |

inter-processor communication. Computed results are presented through the parallel performance of the Taylor–Galerkin scheme over a cluster of $n$-processors, by measuring the total speed-up ($S_n$) factor and efficiency ($\eta_n$) with increasing numbers of processors (and subtasks) define as:

$$S_n = \frac{T_{\text{seq}}}{T_n}, \quad \eta_n = \frac{S_n}{n}$$

where $T_{\text{seq}}$ is the CPU time in seconds (s) for the sequential algorithm and $T_n$ is the CPU time for the parallel algorithm. CPU time $T_n$ of the parallel computation can be decomposed into computation time ($T_n^{\text{comp}}$) and communication time ($T_n^{\text{comm}}$). Timings correspond to total job run-time, inclusive of input–output and communication latency.

In Table VIII, speed-up and efficiency factors are recorded for the parallel Taylor–Galerkin/pressure-correction algorithm. These timings are for Newtonian and viscoelastic simulations on the E-V1S problem with mesh M3, a most detailed case. In our previous investigations [3, 5] we considered large problems, so that for up to twelve processors, linear speed-up was derived and only two percent loss of efficiency was observed. The current problems are particularly chosen to illustrate parallelised performance characteristics over mixed-type computing platforms of up to order 20 processors. The homogeneous network comprises of up to six slave processors and one master processor, from a shared-memory cluster. Quantized metrics on heterogeneous clusters are cross-checked on equivalent homogeneous clusters (same number of processors), demonstrating a degradation of about 1 per cent in time consumption between these network options.

In Figure 14, over a heterogeneous network cluster, timings for Newtonian flows illustrate almost linear speed-up with an increasing number of processors. Only 5 per cent loss of efficiency is observed with up to four processors. As we split our computational domain into more than four subdomains (therefore increasing the number of slave processors), linear speed-up degrades. So for example, on a heterogeneous network cluster of 16 processors, degradation in efficiency is observed by as much as 20 per cent. In this case, interfacing nodes on the master processor exceed the total number of computational nodes on each subdomain.

For viscoelastic computations, on an eight slave- and one master-processor heterogeneous network cluster, 5 per cent loss of efficiency is observed. This performance level is already superceeded for Newtonian simulations once four-slave processors are involved. This reflects the fact that viscoelastic computations carry about two and half times the DOF of the Newto-

 

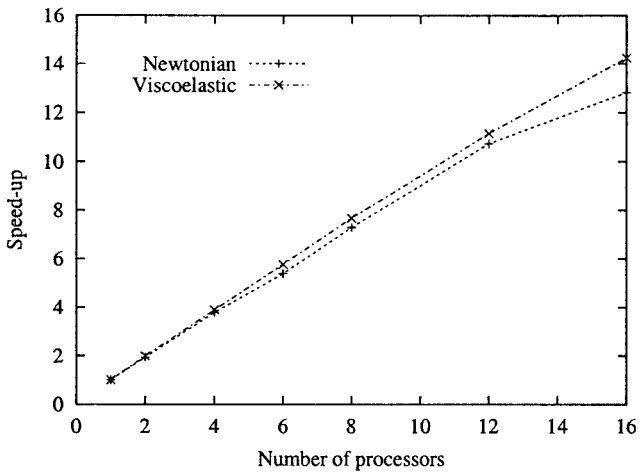


Figure 14. CPU speed-up; heterogeneous cluster.

nian case and hence double $T_n^{\text{comp}}$. The consequence of this loading is felt within our parallel implementation via the ratio of internal to boundary nodes in each instance. This ratio will affect the proportion of cost, split between communication and sub-problem computation (e.g. masking communication [3, 11, 5]).

Clearly, it is preferable to acquire sufficiently large problems to take full advantage of the efficiency offered through parallelization. For optimality, a balance must be struck between the degrees-of-freedom per subdomain and the number of processors $n$. This should ensure that the ratio between $T_n^{\text{comp}}$ and $T_n^{\text{comm}}$ is minimal. For the current problem of E-V1S on mesh-M3, Newtonian results for 8530 nodes and 19 225 DOF reflect a decline in speed-up factor and efficiency on two slave-processors (or subdomains, see Table VIII), tolerating about 2.3 per cent $C_n$ ratio (Table II). For viscoelastic timings with 44 815 DOF, degradation does not emerge until four slave-processors are invoked, for which $C_n$ approaches about 9.9 per cent on the master and 5.2 per cent on the slaves. The more meaningful ratio is held to be the slave $C_n$. This reechos our previous experience [3]. Communication and compute time are not one-to-one in value, being dependent upon different hardware mechanisms. One may identify, for example, an acceptable level of efficiency loss, say O(10 per cent). In this case, to satisfy such a threshold, one would reasonably expect to employ 12 or more processors for the viscoelastic problem and around eight processors for the Newtonian problem. This equates to slave $C_n$ ratios of around 15 per cent for the viscoelastic problem and 10 per cent for the Newtonian case. The overall message is, the larger the $T_n^{\text{comp}}$, the more $T_n^{\text{comm}}$ can be tolerated, and thus masked. The benefit is that ever larger problems are demanded to take full advantage of the parallisation capabilities.

## 7. CONCLUSIONS

For the problems considered, almost linear speed-up is achieved with distributed parallel computation, undertaken over homogeneous and heterogeneous network clusters. This is the

 

case for clusters with up to a score of relatively powerful individual processors (coarse-grained). For viscoelastic simulations, speed-up improves compared to Newtonian and inelastic cases due to the increase in DOF per node, and hence, the relative increase in compute-time for each sub-problem. Practically ideal linear speed-up is identified as attainable, provided certain threshold ratios on problem size per processor are not exceeded. In particular, compute time per processor should be maximised so that communication can be effectively masked.

With respect to the flow problems investigated, we have analysed our results with respect to variation in mixer design (adjusting stirrer shape) and through change of fluid rheology. On rheology, a range of material properties have been investigated, viscous and elastic, covering those for model fluids, model dough, and actual dough. This has lead to analysis with respect to increasing viscosity levels, examination of the influence of viscous to shear-thinning effects, and the incorporation of various levels of fluid memory. We have identified flow structure with variation across problem instances, reflecting localized rate-of-work maxima and global power consumption.

For these rotational flows, about an eccentrically positioned stirrer in a cylindrical vessel, a recirculating region appears towards the centre of the vessel. All three stirrer-shapes, full, horizontal-half and vertical-half, reflect this structure. Decreasing viscosity levels and elevating inertia, distorts the shape of the recirculating region, resulting in asymmetry, and this asymmetric vortex twists and moves towards the upper half-plane of the domain. Such asymmetry is further enhanced through elasticity. The horizontal-half stirrer case manifests more dramatic compression and expansion around both sides of the stirrer, than the alternative geometries. For the vertical-half stirrer as compared to the full case, the flow circumvents the stirrer more smoothly on the side towards the vessel centre, whilst on the counterside of the stirrer, the flow structure emulates that of the full-stirrer.

Overall, we have observed that inertia has a significant influence in disturbing the symmetry in flow structure. Shear-thinning introduces larger shear-rates, but reduces localised rate-of-work maxima and global power. Elasticity also has the effect of destroying flow symmetry. There is an order of magnitude reduction in rate-of-work maxima for viscoelastic fluid-2 above that for viscous fluids-1, and the non-symmetric stirrer cases provide double the values of the full-stirrer instance. Another feature is the wider dispersal of shear-rate and rate-of-work for the viscoelastic fluid. The hoop stress tends to dominate the other components, providing azimuthal stretching. It displays the more prominent and extended wake region beyond the stirrer, in a zone close to the vessel wall occupied by flow lines that encounter the stirrer. Accounting for stress differentials, we observe that the vertical-half stirrer results closely resemble those of the full-stirrer. There is a significant rise from full-stirrer to horizontal-half stirrer flow in both shear and hoop stress differentials: hoop stress differential doubles and shear stress differential triples. Both such quantities will contribute to shear and extensional elastic work, as flow lines become non-circular, say in the vicinity of the stirrer where stress extrema occur.

For model fluids (fluid-3, where viscosity and E are O(1)) and inertia is a factor, the horizontal-half stirrer geometry is the optimal design choice on a $\dot{w}:\dot{P}_w$ rating basis. This preference is quite marked. We have demonstrated that with reduction in elasticity (fluid-3 to fluid-4a), $\dot{\gamma}$ rises by 25 per cent, $\tau_{\theta\theta}$ increases five-fold and $\dot{w}$ increases by about a factor of ten. Global power declines by about one-half, and significantly, power rating ratio increases by one order of magnitude. An increased solvent presence in the modelling does not alter these findings.

 

For dough like fluids (fluid-2), optimal mixer $\dot{w}:\dot{P}_w$ rating resides with the horizontal-half stirrer design, though the reduction to vertical-half stirrer design is only minor. Both unsymmetric stirrer choices double the rating for the full-stirrer design. So for both viscous and elastic fluids, the unsymmetric stirrer option is advocated, with the horizontal-half stirrer the optimal selection with respect to maximising local rate-of-work per unit power. For viscous fluids, this preference is prominent, with power rating ratio doubling for the horizontal-half stirrer design. This is the useful coefficient that dictates quality of kneading work. Through analysing the contributions to elastic rate-of-work, we observe that fluids with memory, as opposed to purely viscous alternatives, are capable of supporting significant extensional localised rate-of-work. We have pointed to where this arises and comment upon its impact upon the kneading process. This is deemed to be of considerable importance to the actual industrial application. Justification for our findings and comparison with experimental data may be gathered through the open literature and the extensive detail we have provided there [33, 34].

To the future, possible extensions to the present work lie in considering variants in rheology and three-dimensional settings (see [1, 2, 5, 35]). The latter is important when it is necessary to consider full flow fields within the mixer-vessel, say under part-filled scenarios. Here, further complexity in boundary conditions (wetting and peeling [2], slip [36], and free-surfaces) and the shear size of the flow problems introduces new and challenging issues to resolve. Efficiency in computation becomes even more critical. Alternative rheology may be addressed also, say through viscoplastic response, which is of wide industrial interest. This may be achieved via a Bingham plastic-type representation with a yield stress (such as, through the Sisko model, an adaptation of the Cross model [37]), an alternative form to the viscous response considered here.

## REFERENCES


1. Sujatha K, Ding D, Webster MF. Modelling three-dimensions mixing flows in cylinder-shaped vessels. In *ECCOMAS CFD—2001*. Swansea: UK, 2001; 1–10.
2. Sujatha K, Ding D, Webster MF. Modelling of dough mixing with free surfaces in two and three dimensions. In *Sixth International Conference on Computational Modelling of Free and Moving Boundary Problems-2001*. Brebbia CA, Sarler B (eds). WIT: Lemnos, Greece, 2001; 102–111.
3. Baloch A, Grant PW, Webster MF. Parallel computation of two-dimensional rotational flows of viscoelastic fluids in cylindrical vessels. *Engineering Computation* 2002; **19**(7):820–853.
4. Xue SC, Phan-Thien N, Tanner RI. Fully three-dimensional, time-dependent numerical simulations of Newtonian and viscoelastic swirling flows in a confined cylinder Part 1. Method and steady flows. *Journal of Non-Newtonian Fluid Mechanics* 1999; **87**:337–367.
5. Baloch A, Grant PW, Webster MF. Homogeneous and heterogeneous distributed cluster processing for two and three-dimensional viscoelastic flows. *International Journal for Numerical Methods in Fluids* 2002; **40**: 1347–1363.
6. Pacheco PS. *Parallel Programming with MPI*. Morgan Kaufmann: Los Altos, CA, 1997.
7. Geist A, Beguelin A, Dongarra J, Jiang W, Manchek R, Sunderam VS. PVM: parallel virtual machine. *A User's Guide and Tutorial for Networked Parallel Computing*. MIT Press: Cambridge, MA, 1994.
8. Keunings R. Parallel finite element algorithms applied to computational rheology. *Computers and Chemical Engineering* 1995; **19**(6–7):647–669.
9. Dou HS, Phan-Thien N. Parallelisation of an unstructured finite volume code with PVM: viscoelastic flow around a cylinder. *Journal of Non-Newtonian Fluid Mechanics* 1997; **77**(1–2):21–51.
10. Grant PW, Webster MF, Zhang X. Solving computational fluid dynamics problems on unstructured grids with distributed parallel processing. In *Parallel Algorithms for Irregularly Structured Problems*, Ferreira A, Rolim J (eds). *Lecture Notes in Computer Science*, vol. 980. Springer: Lyon, France, 1995; 187–197.
11. Grant PW, Webster MF, Zhang X. Coarse-grain parallel finite element simulations for incompressible flows. *International Journal for Numerical Methods in Engineering* 1998; **41**:1321–1337.


 

12. Dris I, Shaqfeh SG. On purely elastic instabilities in eccentric cylinder flows. *Journal of Non-Newtonian Fluid Mechanics* 1995; **56**:349–360.
13. Dris I, Shaqfeh SG. Flow of a viscoelastic fluid between eccentric cylinders: on flow stabilities. *Journal of Non-Newtonian Fluid Mechanics* 1998; **80**:59–87.
14. Li XK, Gwynllyw DR, Davies AR, Phillips TN. On the influence of lubricant properties on the dynamics of two-dimensional journal bearings. *Journal of Non-Newtonian Fluid Mechanics* 2000; **93**(1):29–59.
15. Phan-Thien N, Safari-Ardi M, Morales-Patino A. Oscillatory and simple shear flows of a flour-water dough: a constitutive model. *Rheologica Acta* 1997; **36**(1):38–48.
16. Phan-Thien N, Newberry M, Tanner RI. Non-linear oscillatory flow of a solid-like viscoelastic material. *Journal of Non-Newtonian Fluid Mechanics* 2000; **92**:67–80.
17. Townsend P, Webster MF. An algorithm for the three-dimensional transient simulation of non-Newtonian fluid flows. In *Proceedings of the International Conference on Numerical Methods in Engineering*: *Theory and Applications*, Pande G, Middleton J (eds). NUMETA, Nijhoff: Dordrecht, 1987; T12/1–11.
18. Hawken DM, Tamaddon-Jahromi HR, Townsend P, Webster MF. A Taylor–Galerkin-based algorithm for viscous incompressible flow. *International Journal for Numerical Methods in Fluids* 1990; **10**:327–351.
19. Carew EO, Townsend P, Webster MF. Taylor–Petrov–Galerkin algorithm for viscoelastic flow. *Journal of Non-Newtonian Fluid Mechanics* 1994; **50**:253–287.
20. Baloch A, Townsend P, Webster MF. On the simulation of highly elastic complex flows. *Journal of Non-Newtonian Fluid Mechanics* 1995; **59**:111–128.
21. Matallah H, Townsend P, Webster MF. Recovery and stress-splitting schemes for viscoelastic flows. *Journal of Non-Newtonian Fluid Mechanics* 1998; **75**:139–166.
22. Sloan SW. An algorithm for profile and wavefront reduction of sparse matrices. *International Journal for Numerical Methods in Engineering* 1986; **23**:239–251.
23. Simon HD. Partitioning of unstructured problems for parallel processing. *Computer Systems in Engineering* 1991; **2**:135–148.
24. Matallah H, Townsend P, Webster MF. Viscoelastic multi-mode simulations of wire-coating. *Journal of Non-Newtonian Fluid Mechanics* 2000; **90**:217–241.
25. Ngamaramvaranggul V, Webster MF. Simulation of pressure-tooling wire-coating flow with Phan-Thien/Tanner models. *International Journal for Numerical Methods in Fluids* 2002; **38**:677–710.
26. Aboubacar M, Matallah H, Webster MF. Highly elastic solutions of Oldroyd-B and Phan-Thien/Tanner fluids with a hybrid finite volume/element method: planar contraction flows. *Journal of Non-Newtonian Fluid Mechanics*, 2002; **103**:65–103.
27. Tanner RI. *Engineering Rheology* (2nd edn). Oxford University Press: Oxford, 2000.
28. Keunings R. Simulation of viscoelstic flow. In *Computer Modeling for Polymer Processing*, Tucker CL (ed.). Hanser: Munich, 1989.
29. Baaijens FPT. Mixed finite element methods for viscoelastic flow analysis: a review. *Journal of Non-Newtonian Fluid Mechanics* 1998; **79**:361–385.
30. Walters K, Webster MF. The distinctive CFD challenges of computational rheology: keynote. *International Journal for Numerical Methods in Fluids* 2003; **43**:577–596 (special issue).
31. Mutlu I, Townsend P, Webster MF. Simulation of cable-coating viscoelastic flows with coupled and decoupled schemes. *Journal of Non-Newtonian Fluid Mechanics* 1998; **74**:1–23.
32. Schoonen JRM, Swartjes FHM, Peters GWM, Baaijens FPT, Meijer HEH. A 3D numerical/experimental study on a stagnation flow of a polyisobutylene solution. *Journal of Non-Newtonian Fluid Mechanics* 1998; **79**: 529–561.
33. Sujatha KS, Webster MF, Binding DM, Couch MA. Modelling and experimental studies of rotating flows in part-filled vessels: wetting and peeling. *Journal of Food Engineering* 2003; **57**:67–79.
34. Binding DM, Couch MA, Sujatha KS, Webster MF. Experimental and numerical simulation of dough kneading in filled geometrics. *Journal of Food Engineering* 2003; **58**:111–123.
35. Ding D, Webster MF. Three-dimensional numerical simulation of dough kneading. In *XIII International Congress on Rheology*, vol. 2, Binding D, Hudson N, Mewis J, Piau J-M, Petrie C, Townsend P, Wagner M, Walters K (eds). British Society of Rheology: Cambridge, UK, 2000; 318–320.
36. Ngamaramvaranggul V, Webster MF. Viscoelastic simulations of stick-slip and die-swell flows. *International Journal for Numerical Methods in Fluids* 2001; **36**:539–595.
37. Barnes HA, Hutton JF, Walters K. *An Introduction to Rheology*. Elsevier: Amsterdam, 1989.

 